Article type: Original paper

1064 nm acoustic resolution photoacoustic microscopy

Vijitha Periyasamy[1], *Nandan Das*[1,2], *Arunima Sharma*[1], *and Manojit Pramanik*[1,*]

*Corresponding Author: E-mail: manojit@ntu.edu.sg, Phone: +6567905835, Fax: +65 67911761

[1]School of Chemical and Biomedical Engineering, Nanyang Technological University, Singapore 637459

[2]Present affiliation: Tissue Optics & Microcirculation Imaging Group, School of Physics, National University of Ireland, Galway, Ireland

Keywords: (Acoustic resolution photoacoustic microscopy, photoacoustic imaging, sentinel lymph node, urinary bladder, deep tissue imaging)

Photoacoustic imaging is a non-invasive imaging technique having the advantages of high optical contrast and good acoustic resolution at improved imaging depths. Light transport in biological tissues is mainly characterized by strong optical scattering and absorption. Photoacoustic microscopy is capable of achieving high resolution images at greater depth compared to conventional optical microscopy methods. In this work, we have developed a high-resolution, acoustic resolution photoacoustic microscopy (AR-PAM) system in the near infra-red (NIR) window II (NIR-II, e.g., 1064 nm) for deep tissue imaging. Higher imaging depth is achieved as the tissue scattering at 1064 nm is lesser compared to visible or near infrared window-I (NIR-I). Our developed system can provide a lateral resolution of 130 µm, axial resolution of 57 µm, and image up to 11 mm deep in biological tissues. This 1064-AR-PAM system was used for imaging sentinel lymph node and the lymph vessel in rat. Urinary bladder of rat filled with black ink was also imaged to validate the feasibility of the developed system to study deeply seated organs.

1. Introduction:

Photoacoustic imaging (PAI) is a promising non-invasive imaging technique based on ultrasound detection generated by the tissue chromophores when excited with nanosecond laser pulses.[1-4] Absorption of laser pulses by the tissue chromophores results in local temperature rise, which causes thermoelastic expansion and therefore, generation of photoacoustic (PA) waves. The generated PA waves are then detected by broadband ultrasound transducer (UST).[5] This gives PAI the advantages of both high optical contrast and high ultrasound resolution. Images of biological entities can be collected using PAI with consistent contrast across the range from organelles to organs.[6] PAI techniques are safe, non-invasive, and non-ionizing and can provide various anatomical and functional information such as vascular structure, angiogenesis of tumors, oxy- and deoxy-hemoglobin concentration, total hemoglobin concentration, blood flow speed, temperature in tissue, rate of oxygen metabolism etc.[7, 8] Photoacoustic molecular imaging is also becoming very popular, especially with the use of targeted contrast agents.[9-12]

PAI can be broadly classified as photoacoustic tomography/photoacoustic computed tomography, (PAT/PACT) and photoacoustic microscopy (PAM). In PAT/PACT, the laser illuminates the sample homogeneously and single or multiple USTs are used to collect PA signals from around the sample.[13] Then, reconstruction algorithms are used to process the collected PA signals to provide cross-sectional images of the target.[14, 15] On the other hand, in PAM, a confocal optical excitation and ultrasonic detection is used to provide higher resolution compromising the imaging depth (in comparison to PAT/PACT). PAM systems perform raster scan of the optical and acoustic foci over the sample to acquire three dimensional volumetric information of the target sample.[16-18] They are further classified as optical resolution photoacoustic microscopy (OR-PAM)[19] and acoustic resolution

photoacoustic microscopy (AR-PAM).[20] In OR-PAM, a tight optical focus (using an objective with high numerical aperture) determines the lateral resolution of the imaging system. However, the imaging depth in OR-PAM is still limited to the optical mean-free path of ~1 mm in biological tissues.[21, 22] Limitation of shallow imaging depth can be overcome by using AR-PAM, but with a compromise on the spatial resolution due to weak optical focus used in those systems. In AR-PAM the lateral resolution is mainly decided by the ultrasound focus. AR-PAM systems generally employ dark-field light illumination (donut-shaped beam to minimize signal from tissue surface) and high numerical aperture USTs for detection of PA signal.[23] In both OR- and AR-PAM the axial resolution is determined by the bandwidth of the UST used for PA signal acquisition.

Although AR-PAM can provide better resolution as compared to PAT, imaging depth is generally reduced. Favazza *et al.*, developed a dual wavelength (560 nm and 571 nm) AR-PAM system for microvascular imaging of human palm.[24] They achieved ~70 µm lateral resolution and 54 µm axial resolution. Moothanchery *et al.* demonstrated a switchable AR-OR-PAM system (operated at 570 nm) wherein the AR-PAM set-up achieved 45 µm lateral resolution and 33 µm axial resolution at an imaging depth of 4.6 mm.[16] Song *et al.*, achieved an imaging depth of 19 mm with an AR-PAM system of 804 nm light excitation source, but the lateral resolution was sacrificed to 560 µm and the axial resolution to 144 µm, due to the use of low frequency (5 MHz focused) UST.[25] AR-PAM systems reported so far have used laser pulses of visible or near infrared (NIR-I) wavelengths.[18, 26, 27] Such systems have found their applications in tumor imaging, sentinel lymph node imaging, imaging of vasculature etc.[26, 28-30] Jeon *et al.*, demonstrated multiplane whole body imaging at 532, 700, 850, and 1064 nm wavelengths using 5 MHz and 40 MHz transducers.[31] However, no AR-PAM system with a resolution in the order of hundreds of

micrometer with more than 10 mm imaging depth in biological tissues has been reported so far. Achieving higher depth with visible or NIR-I window is challenging due to the high attenuation of light by skin and other surface tissues.[32]

Near infra-red window II (NIR-II, e.g., 1064 nm) has been recently used in PAT imaging because it penetrates deeper into tissue.[33-38] Even 1064 nm OR-PAM is demonstrated with deep imaging depth compared to traditional OR-PAM.[19, 39] However, no work has been done in AR-PAM dedicated to NIR-II window. Attenuation of the 1064 nm laser pulses by skin is three orders less as compared to that of laser pulses in visible range. Therefore, 1064 nm laser makes it possible to penetrate deeper and thus perform deep tissue imaging.[40-42] Another advantage of NIR-II imaging window is that higher laser energy can be used for illumination compared to visible or NIR-I window. As per American National Standards Institute (ANSI), maximum permissible energy for skin is 1 W/cm^2 at 1064 nm compared to 200 mW/cm^2 at 532 nm or 300 mW/cm^2 at 800 nm for illumination of more than 10 seconds.[43] Recently, higher wavelengths are being used for photoacoustic imaging of palm vasculature and other applications in human, such as tattoo removal.[44, 45]

In this work, we have designed an AR-PAM system where the illumination source is 1064 nm pulsed laser (1064-AR-PAM). This is the first report of using NIR-II wavelength laser (1064 nm) to do AR-PAM using high frequency ultrasound transducer with improved imaging depth. Compared to the usual PAT/PACT systems (which use NIR-I and NIR-II wavelength), this system can provide better resolution with reasonable imaging depth and compared to other AR-PAM or OR-PAM systems this system can provide higher imaging depth with good spatial resolution. Our developed system is characterized using carbon microsphere for spatial resolution and the depth of imaging is quantified using a black tape

phantom. Feasibility of the 1064-AR-PAM system for *in vivo* imaging is demonstrated by imaging sentinel lymph node and urinary bladder of rats.

2. Materials and Methods:

2.1. 1064-AR-PAM System:

Figure 1 shows the schematic of the 1064-AR-PAM system. 1064 nm laser pulses were generated by nanosecond diode-pumped solid-state Nd:YAG laser (INNOLASAB, Edgewave, Wurselen, Germany). Laser beam was passed through the lenses L1 (LJ1328L2-B, Thorlabs, Newton, NJ, USA) and L2 (LA1257-C, Thorlabs) to collimate the beam. Filter (FGS900-A, Thorlabs) removed the residual 532 nm beam. The resultant beam was passed through variable neutral density filter (NDC-50C-4M, Thorlabs) to control the illumination energy on the sample. Lens L3 (LA1257-C, Thorlabs) was used to focus the laser beam into the multi-mode fiber (MHP910L02, Thorlabs) mounted on the linear translation stage (XYT1, Thorlabs). The output end of the fiber tip was connected to the fiber-tip holder mounted on a 60 mm cage (which was designed as scanning head) for better alignment and easy movement. Damage threshold of this fiber is ~50W @ 980 nm. In the current set-up 12 W was delivered to the fiber input end and 9 W was received at the output end of the fiber. Laser beam from the fiber-tip was converted to a ring-shaped beam using a focusing lens, L4 (LA1951, Thorlabs) and a conical lens of apex angle 130º, CL (1-APX-2-B254, Altechna, Vilnius, Lithuania) which were mounted on a translation stage (CT1, Thorlabs). The ring-shaped beam was passed through a homemade optical condenser (acrylic) of cone angles 75º and 105º. The condenser housed a 30 MHz ultrasound transducer (V214-BB-RM, Olympus-NDT, Waltham, MA, USA). A diverging lens (LC1975-C, Thorlabs) of diameter 6 mm and radius of curvature 12.4 mm was attached to the transducer using a UV curing optical adhesive (NOA61, Thorlabs) to get an acoustic focal diameter of ~80 µm. The working

distance of 1064-AR-PAM was 15 mm. In an optically clear medium the optical focus was around ~4 mm in diameter which was higher than the acoustic focal diameter.

The scanning set-up was mounted on a 3-axis motorized stage (PLS 85 for X and Y axis, VT 80 for Z axis, PI-Physik Instrumente, Karlsruhe, Germany) which was controlled by a 3-axis controller (SMC corvus eco, PI micos). The scanning head was immersed in a water tank (13 cm × 30 cm) with a membrane window of diameter 10 cm for acoustic coupling. Clear ultrasound gel was used to couple the sample and imaging window. The signal from the transducer was amplified using two serially connected amplifiers each having 24 dB gain (ZFL-500LN, Mini Circuits, Brooklyn, NY, USA), and then acquired by data acquisition (DAQ) card (M4i.4420, Spectrum, Grosshansdorf, Germany) installed in a desktop (Intel xeon E5-1630 3.7 GHz processor, 16 GB RAM, 64 bit windows 10 operating system). The two channel DAQ card had a sampling rate of 250 Megasamples/second, 16 bit analog-to-digital converter, and 4 GB on-board memory. A function generator (GW INSTEK, AFG-3051) triggered and synchronized the laser with DAQ. Labview software (National Instrument) was used as a user interface. The scanning head was raster scanned over the sample to acquire A-lines. For our experiments, the step-size was 30 µm and 3 µm along x-axis and y-axis, respectively. Following acquisition, Hilbert transformation was performed on the depth resolved PA signals (A-lines), which were further post-processed to form maximum amplitude projection (MAP) and depth-encoded MAP (DE-MAP) images using MATLAB (MathWorks, Natick, MA, USA).

2.2. Laser safety limits:

Nd:YAG laser was operated at a pulse repetition rate (PRR) of 5 kHz and the energy on the sample was 1.8 mJ/pulse. According to ANSI safety limit,[43] maximum permissible

exposure (MPE) for skin for exposure time of less than 10 sec is 1.1 $C_A\, t^{0.25}\, J/cm^2$, where C_A is a wavelength dependent factor, and t is the time of exposure. Since the diameter of optical focus at ultrasound focus was approximately 4 mm and the minimum pixel separation was 3 µm, 1333 continuous pulses were illuminating at each point. Therefore, for a PRR of 5 kHz, the exposure time was 267 ms, making the MPE for our system 3.95 J/cm^2. For a sample getting exposed to 1333 pulses, the allowed MPE per pulse becomes 2.96 mJ/cm^2. For our experiments, a maximum energy of ~1.8 mJ per pulse illuminated an area of ~1.75 cm^2 on skin (assuming a ring shaped beam with outer and inner diameter of 15 and 13 mm, respectively), making the per pulse laser energy ~1 mJ/cm^2, thereby maintaining it below the ANSI safety limit.

2.3. System characterization:

The developed system was characterized using carbon microspheres and United States Air Force (USAF) 1951 resolution test target. First, the lateral resolution of the system was characterized using 2-12 µm carbon sphere (7440440, Aldrich). The spheres were suspended in tween-20 (9005645, Sigma Aldrich) to avoid aggregation of the particles. The suspended solution was smeared on a microscope glass slide and placed under the imaging window. A single microsphere was imaged using the 1064-AR-PAM system. A profile was extracted along the center of the particle from its MAP image. The extracted profile was fitted with a Gaussian curve. The full width at half maximum (FWHM) of such Gaussian fit gives the lateral resolution of the system. Theoretically, the lateral resolution of the AR-PAM is given by $0.71\,\lambda/NA$, where λ is the central wavelength of the UST and NA is the numerical aperture of the UST. The microsphere was scanned up to 2 mm above and below the focal plane in steps of 0.5 mm. 3 mm thick chicken breast was positioned on the membrane in the water tank to diffuse the light to the sample. Gaussian curve was fit along the lateral axis of

the sphere in the nine scans. This provides the system resolution at different depths. Axial resolution of the system was calculated from the axial spread profile of the PA signal from the carbon microsphere. Since the carbon microsphere was a few microns thick, the A-line of the microsphere can be approximated to a point source profile. FWHM of the envelope of the PA signal gives the axial resolution of the developed system. Axial resolution of PA microscopy is theoretically given by $0.88v_A/\Delta f_A$ where, v_A is the speed of sound in the medium and f_A is the bandwidth of the UST.

USAF test target (R1DS1P, Thorlabs) was imaged to further validate the scanning of the system. Group numbers 0 and 1 were imaged whose line widths vary from 400 µm to 140 µm. The target was scanned along x-axis and y-axis (20 mm × 20 mm) which also covered groups 2 and 3. Modulation transfer function (MTF) was computed across the group 2, element 4 with line width 99.2 µm. $MTF = (I_{max} + I_{min})/(I_{max} - I_{min})$ where I_{max} was the maximum intensity in the region of interest and I_{min} was the minimum intensity in the background. MTF is an estimate of the relative contrast. Next, a phantom study was conducted to validate the depth of imaging. A black tape was inserted at an angle inside chicken breast tissue. 100 scans of a plane perpendicular to the black tape were acquired and averaged. Signal to noise ratio (SNR), which is $20log_{10}(V/n)$, where V is average of PA signal at the maximum imaging depth and n is the standard deviation of the background noise, was calculated for this averaged data.

2.4. In vivo imaging:

The feasibility of 1064-AR-PAM for small animal imaging was tested by imaging the sentinel lymph node (SLN) and the urinary bladder of rat. *In vivo* experiments were performed in accordance to the guidelines and regulations approved by the Institutional

Animal Care and Use Committee of Nanyang Technological University, Singapore (Animal Protocol Number ARF-SBS/NIE-A0263). Rats (procured from InVivos Pte Ltd) were anesthetized using a cocktail of ketamine and xylazine of dosage of 85 and 15 mg/kg, respectively before experimentation. 0.2 mL of the mixture per 100 gms of the rat body weight was injected intraperitoneally. 0.75% of isoflurane gas (Medical Plus Pte Ltd, Singapore) along with oxygen (1.2 L/min) was administered through custom made nose cone to maintain the animals in anaesthesia during the scanning. The vitals of the animals were monitored using pulse oximeter (Medtronic, PM10N with veterinary sensor, Minneapolis, Minnesota, USA) which was clipped to the hind-paw.

A 75 gms adult female Sprague Dawley rat was used for the sentinel lymph node imaging. The hair above the forepaw of the animal was depleted using commercially available hair removal cream. An area of 20 mm × 20 mm was scanned above the fore-paw. 0.2 mL of contrast agent (black ink) was injected in the forepaw of the rat. The post-injection scan was acquired in the region similar to the pre-injection scan. A 150 gms adult male Sprague Dawley rat was used for the urinary bladder imaging. The hair on the abdomen of the rat was depleted when the rat was under the influence of anaesthesia and a 23G urinary bladder catheter was inserted into the urethra and glued to the skin using tissue glue. The pre-injection and the post-injection scans were acquired before and after injecting 1 mL of black ink. After the experiments, the rats were euthanized with an overdose of pentobarbital. Once the death of the animal was ensured, the skin was surgically removed to expose the area of interest.

3. Results and discussions:

We have shown the experimental lateral and axial resolution of the developed 1064- AR-PAM system in **Figure 2**. **Figure 2(a)** shows the lateral resolution of the system. Inset is the MAP of the microsphere and the plot (shown as dots) is the profile along the center of the sphere. The solid line in the graph represents the Gaussian fit. The lateral resolution computed from the Gaussian fit is 130 µm. The experimentally determined resolution correlates well with the theoretical calculation of ~121 µm (acoustic NA was 0.3). **Figure 2(b)** is the lateral resolution of the system at various depths around the focal plane. The dots are the experimental values and solid line is the Gaussian fit. The resolution degrades away from the focus as expected. Resolution is approximately 180 µm 2 mm away from the focal plane. **Figure 2(c)** is the A-line of the PA signal generated from the microsphere and its envelope. Experimentally, the axial resolution is found to be ~57 µm which is close to the theoretical value of ~52 µm (for v_A = 1540 m/s and Δf_A = 26 MHz). The lateral resolution, axial resolution, and depth of imaging of various systems are compared with this developed system and are summarized in Table 1.

In **Figure 3**, we have demonstrated resolving power and maximum depth of imaging using USAF test target and black tape phantom. **Figure 3(a)** shows the MAP image of USAF test target. It is seen that the lines of group 2 element 2, which are of size 125 µm are resolved. The profile along the group 2, element 2 to 4 is shown in **Figure 3(b)**. It is seen that the elements of width 125 µm to 99 µm are resolved. The MTF of element 4 is 0.54. **Figure 3(c)** is the averaged B-scans (A-lines along the y-axis) of the black tape phantom. It is clearly seen that the system can image till a depth of 11 mm (when the focus is 5 mm below the tissue surface) with acceptable signal strength. The SNR at 11 mm is 58 dB.

Figure 4 is the illustration of the *in vivo* sentinel lymph node imaging of the rat. **Figure 4(a)** is the photograph of the animal before injection. **Figure 4(b)** is the MAP photoacoustic image of pre-injection from the 1064-AR-PAM system. **Figure 4(c)** and **Figure 4(d)** are the MAP and DE-MAP images of the sentinel lymph node, respectively. Lymph vessels are also visible in the MAP image validating the resolution of the developed system for *in vivo* imaging. The lymph vessel structure seen in MAP correlates well with the flow of the black ink observed in the photograph taken after the imaging was done and the animal was sacrificed and the SLN area was exposed surgically [Figure 4(e)]. The structure of the lymph node in MAP is similar to the shape of the dissected lymph node as shown in **Figure 4(f)**.

Figure 5 is the illustration of the *in vivo* urinary bladder imaging of the rat. **Figure 5(a)** is the photograph of abdomen of the rat after hair depletion. The PA images acquired pre and post injection are shown in **Figure 5(b)** and **Figure 5(c)**, respectively. The depth encoded MAP image is shown in **Figure 5(d)**. The catheter is inserted into the urinary bladder as shown in the **Figure 5(e)**. The diameter of the urinary bladder estimated from the MAP is approximately 5 mm which is similar to what is seen in the excised urinary bladder (after PA imaging was complete and the animal was sacrificed) in **Figure 5(f)**. Imaging of urinary bladder validates the *in vivo* depth of imaging of 1064-AR-PAM system.

In summary, we have developed NIR-II window based reflection mode AR-PAM system for deep tissue imaging at high resolution. A lateral resolution of ~130 µm and an axial resolution of ~57 µm at an imaging depth of 11 mm could be achieved using the system. *In vivo* images acquired using this system substantiate its applications in biomedical imaging. Furthermore, since the wavelength of 1064 nm is generated by Nd:YAG pump lasers, this configuration is both cost effective and compact in size as compared to NIR-I laser based

systems. The developed 1064-AR-PAM system can further be modified and then applied for various pre-clinical and clinical applications. Optimization of central frequency of UST can be done to extend the imaging depth or the system resolution according to the desired application. The 30 MHz transducer used in this set-up increases the depth of imaging without the compromise in the resolution of the system. Imaging depth may further be increased by decreasing the central frequency of transducer used. However, this may result in poor spatial resolution. It is to be noted that, 5 MHz transducer used for 804 nm AR-PAM system has a resolution of 560 µm at the imaging depth of 19 mm. Also note that, the blood vessel structures are not as clearly visible as reported by systems using visible or NIR-I wavelength as excitation. This is probably due to the poor light absorption of 1064 nm wavelength compared to visible or NIR-I. Blood absorbs nearly 100 times more in the visible and 10 times more in the NIR-I (800 nm) region compared to NIR-II (1064 nm) region. Thus the initial pressure rise in surrounding tissue and blood is not significantly high and as a result the blood vessels are not very clearly visible in NIR-II window with the microscopic systems.[46] Moreover, reconstruction algorithms to improve out-of-focus resolution can further be implemented to enhance the image quality.[47] Signal to noise ratio can be increased if the surface of the transducer is manufactured concave rather than gluing the concave lens to the transducer. However, gluing of lens is a cost-effective solution (rather than making a custom made UST), and therefore may be preferred in some cases. Contrast of the 1064 AR-PAM images can be further improved by increasing the energy of illumination. The energy deposited on the tissue can be increased further without any modification in the system components which would further enhance the imaging contrast and depth. At present only half on the maximum permissible energy is used on the sample surface. The coupling medium (water) used here also absorbs light passing through it. Air-coupled ultrasound

transducers or dry coupling medium are the other options to try to reduce the loss of laser energy in the coupling medium.[48]

In addition, use of black ink (not biocompatible) can be avoided by developing and using biocompatible contrast agents with absorption peak around 1064 nm. It is to be noted the absorbance of black ink is ~5 times that of blood. Although, contrast agents reported so far are majorly in the NIR-I window,[49] there has been a recent boost in research on NIR-II contrast agents.[33-35, 50, 51] Reduction in scanning time (which is currently ~30 minutes for *in vivo* imaging of an area of 2 x 2 cm) with the use of techniques such as galvo-mirrors, 2D acousto optical deflector, or MEMs mirrors, might be possible.[52-54] Execution of the mentioned methods to improve the imaging system is a part of our future work. The advantages of the system such as NIR-II wavelength excitation, higher resolution, and higher imaging depth can be exploited to image deeply seated tumors. Recent progress on the contrast agent development for the NIR-II window can also be exploited with this system for even deeper, higher contrast imaging.

4. Conclusion:

We have developed AR-PAM system and demonstrated the feasibility of NIR-II window (1064 nm) for acoustic resolution imaging. The ability of 1064 nm wavelength to penetrate deeper compared to visible wavelengths has been exploited in this set-up. Custom-made optical condenser is modified to focus the light at a depth of 15 mm by dark-field illumination. The developed system has high resolution (130 μm) imaging capability and an imaging depth of 11 mm. Application of this system for sentinel lymph node imaging in rat has been shown. The flow of the contrast agent in the lymph vessel is also seen in the image, confirming that high resolution imaging of lymph vessels can be performed using this system.

Such depth encoded images can be used for non-invasive imaging of lymph vessels for cancer detection or guiding needle for aspiration biopsy. Black ink was also injected in one of the deeply seated organ, urinary bladder (which is ~1 cm below the skin surface). Image of urinary bladder convinces the use of the developed system for photoacoustic cystography. Certain modifications like use of focused transducer, better reconstruction algorithms, increase the illumination energy, etc. can be done to further improve the 1064-AR-PAM system.

Acknowledgements:

The authors would like to acknowledge the financial support from Tier 2 grant funded by the Singapore Ministry of Education Tier-2 Academic Research Funds (ARC2/15: M4020238). Authors would like to acknowledge Dr. Rhonnie Austria Dienzo for his help with animal experiments. Authors have no relevant financial interests in the manuscript and no other potential conflicts of interest to disclose.

Author biographies

Please see Supporting Information online.

References

[1] L. Li, L. Zhu, C. Ma, L. Lin, J. Yao, L. Wang, K. Maslov, R. Zhang, W. Chen, J. Shi *Nature Biomedical Engineering*. **2017**, *1*, 0071.

[2] P. K. Upputuri, M. Pramanik *J. Biomed. Opt.* **2017**, *22*, 041006.

[3] L. V. Wang, J. Yao *Nat Methods*. **2016**, *13*, 627-638.

[4] S. Manohar, D. Razansky *Advances in Optics and Photonics*. **2016**, *8*, 586-617.

[5] V. G. Andreev, A. A. Karabutov, A. A. Oraevsky *IEEE Transactions on Ultrasonics, Ferroelectrics, and Frequency Control*. **2003**, *50*, 1383-1390.

[6] L. V. Wang, S. Hu *Science*. **2012**, *335*, 1458-1462.

[7] Q. Zhang, N. Iwakuma, P. Sharma, B. M. Moudgil, C. Wu, J. McNeill, H. Jiang, S. R. Grobmyer *Nanotechnology*. **2009**, *20*, 395102.

[8] M. Pramanik, L. V. Wang *J. Biomed. Opt.* **2009**, *14*, 054024.

[9] J. Yao, L. V. Wang *Curr. Opin. Chem. Biol.* **2018**, *45*, 104-112.

[10] T. Stahl, R. Bofinger, I. Lam, K. J. Fallon, P. Johnson, O. Ogunlade, V. Vassileva, R. B. Pedley, P. C. Beard, H. C. Hailes, H. Bronstein, A. B. Tabor *Bioconjug. Chem.* **2017**, *28*, 1734-1740.

[11] D. Pan, M. Pramanik, A. Senpan, J. S. Allen, H. Zhang, S. A. Wickline, L. V. Wang, G. M. Lanza *FASEB J.* **2011**, *25*, 875-882.

[12] D. Razansky, M. Distel, C. Vinegoni, R. Ma, N. Perrimon, R. W. Köster, V. Ntziachristos *Nat Photonics*. **2009**, *3*, 412-417.

[13] P. K. Upputuri, M. Pramanik *J. Biomed. Opt.* **2017**, *22*, 090501.

[14] N. Awasthi, S. K. Kalva, M. Pramanik, P. K. Yalavarthy *J. Biomed. Opt.* **2018**, *23*, 071204.

[15] S. K. Kalva, M. Pramanik *J. Biomed. Opt.* **2016**, *21*, 086011.

[16] M. Moothanchery, M. Pramanik *Sensors*. **2017**, *17*, 357.

[17] M. Moothanchery, R. Z. Seeni, C. Xu, M. Pramanik *Biomed. Opt. Express*. **2017**, *8*, 5483-5492.

[18] J. Yao, L. V. Wang *Laser & Photonics Reviews*. **2013**, *7*, 758-778.

[19] P. Hai, J. Yao, K. I. Maslov, Y. Zhou, L. V. Wang *Opt. Lett.* **2014**, *39*, 5192-5195.

[20] S. Park, C. Lee, J. Kim, C. Kim *Biomedical Engineering Letters*. **2014**, *4*, 213-222.

[21] J. Y. Kim, C. Lee, K. Park, G. Lim, C. Kim *Sci. Rep.* **2015**, *5*, 07932.

[22] W. Song, W. Zheng, R. Liu, R. Lin, H. Huang, X. Gong, S. Yang, R. Zhang, L. Song *Biomed. Opt. Express*. **2014**, *5*, 4235-4241.

[23] K. Maslov, G. Stoica, L. V. Wang *Opt. Lett.* **2005**, *30*, 625-627.

[24] C. P. Favazza, L. A. Cornelius, L. V. Wang *J. Biomed. Opt.* **2011**, *16*, 026004.

[25] K. H. Song, L. V. Wang *J. Biomed. Opt.* **2007**, *12*, 060503.

[26] Z. Guo, Y. Li, S.-L. Chen *Opt. Lett.* **2018**, *43*, 1119-1122.

[27] M. Erfanzadeh, P. D. Kumavor, Q. Zhu *Photoacoustics*. **2018**, *9*, 1-9.

[28] T. Chuangsuwanich, M. Moothanchery, A. T. C. Yan, L. Schmetterer, M. J. A. Girard, M. Pramanik *Appl. Opt.* **2018**, *57*, 4865-4871.

[29] Y. Zhou, J. Yao, L. V. Wang *J. Biomed. Opt.* **2016**, *21*, 061007.

[30] J. Koo, M. Jeon, Y. Oh, H. W. Kang, J. Kim, C. Kim, J. Oh *Phys. Med. Biol.* **2012**, *57*, 7853.

[31] M. Jeon, J. Kim, C. Kim *Med. Biol. Eng. Comput.* **2016**, *54*, 283-294.

[32] G. Ku, X. Wang, G. Stoica, L. V. Wang *Phys. Med. Biol.* **2004**, *49*, 1329-1338.

[33] Z. Wang, P. K. Upputuri, X. Zhen, R. Zhang, Y. Jiang, X. Ai, Z. Zhang, M. Hu, Z. Meng, Y. F. Lu, Y. Zheng, K. Pu, M. Pramanik, B. Xing *Nano Research*. **2018 (In Press)**.

[34] P. K. Upputuri, C. Yang, S. Huang, K. Wang, M. Wang, M. Pramanik *J. Biomed. Opt.* **2018**, *24*, 031002.

[35] J. Zhou, Y. Jiang, S. Hou, P. K. Upputuri, D. Wu, J. Li, P. Wang, X. Zhen, M. Pramanik, K. Pu, H. Duan *Acs Nano*. **2018**, *12*, 2643-2651.

[36] Y. Liu, L. Zhang, S. Li, X. Han, Z. Yuan *Journal of biophotonics*. **2018**, e201700267.

[37] B. C. Wilkinson, T. C. Sheehan, T. Buma *Proc. IEEE Inter. Ultra. Symp.* **2014**, 25-28.

[38] G. Ku, M. Zhou, S. Song, Q. Huang, J. Hazle, C. Li *Acs Nano*. **2012**, *6*, 7489-7496.

[39] N. Q. Bui, S. W. Cho, M. S. Moorthy, S. M. Park, Z. Piao, S. Y. Nam, H. W. Kang, C. S. Kim, J. Oh *Sci. Rep.* **2018**, *8*, 2000.

[40] K. Sivasubramanian, V. Periyasamy, R. A. Dienzo, M. Pramanik *Journal of biophotonics*. **2018**, *11*, e201700317.

[41] Kimberly Homan, Seungsoo Kim, Yun-Sheng Chen, Bo Wang, Srivalleesha Mallidi, S. Emelianov *Opt. Lett.* **2010**, *35*, 2663-2669.

[42] W.-F. Cheong, S. A. Prahl, A. J. Welch *IEEE J. Quantum Electron.* **1990**, *26*, 2166-2185.

[43] *ANSI Standard Z136.1-2007, NY*. **2007**.

[44] Z. Shoujun, Y. Qinglai, L. A. Alexander, Y. Jingying, M. Zhuoran, W. Huasen, H. Wei, W. Hao, W. Joy, D. Shuo, Z. Bo, L. Xiaoyang, Z. Yeteng, Y. Kuai, H. Guosong, L. Jian, L. Yongye, D. Hongjie *Proc. Natl. Acad. Sci. USA*. **2017**, *114*, 962-967.

[45] A. L. Antaris, H. Chen, K. Cheng, Y. Sun, G. Hong, C. Qu, S. Diao, Z. Deng, X. Hu, B. Zhang, X. Zhang, O. K. Yaghi, Z. R. Alamparambil, X. Hong, Z. Cheng, H. Dai *Nature materials*. **2016**, *15*, 235-242.

[46] H. Kang, S. W. Lee, S. M. Park, S. W. Cho, J. Y. Lee, C. S. Kim, T. G. Lee *Journal of biophotonics*. **2018**, *11*, e201700210.

[47] H. Estrada, J. Rebling, D. Razansky *Phys. Med. Biol.* **2017**, *62*, 4728-4740.

[48] X. L. Dean-Ben, G. A. Pang, F. M. de Espinosa, D. Razansky *Appl Phys Lett*. **2015**, *107*, 051105.

[49] C. Kim, C. Favazza, L. V. Wang *Chem. Rev.* **2010**, *110*, 2756-2782.

[50] Z. Chen, X. L. Deán-Ben, S. Gottschalk, D. Razansky *Biomed. Opt. Express*. **2018**, *9*, 2229-2239.

[51] J. Wu, L. You, L. Lan, H. J. Lee, S. T. Chaudhry, R. Li, J. X. Cheng, J. Mei *Adv Mater*. **2017**, *29*, 1703403.

[52] K. Xiong, S. Yang, X. Li, D. Xing *Opt. Lett.* **2018**, *43*, 1846-1849.

[53] H. Guo, C. Song, H. Xie, L. Xi *Opt. Lett.* **2017**, *42*, 4615-4618.

[54] S. Han, C. Lee, S. Kim, M. Jeon, J. Kim, C. Kim *Appl Phys Lett*. **2013**, *103*, 203702.

[55] C. Kim, E. C. Cho, J. Chen, K. H. Song, L. Au, C. Favazza, Q. Zhang, C. M. Cobley, F. Gao, Y. Xia, L. V. Wang *Acs Nano*. **2010**, *4*, 4559-4564.

Table 1: Comparison of performance of acoustic resolution photoacoustic microscopy systems in various wavelengths.

Wavelength (nm)	Transducer center frequency (MHz)	Lateral resolution (µm)	Axial resolution (µm)	Imaging Depth (mm)	Reference
532. 700, 850, 1064	5	590	150	10.3	[31]
532. 700, 850, 1064	40	85	50	3.1	[31]
570	50	45	15	3.1	[55]
778	10	140	125	-	[55]
804	5	560	150	30	[25]
1064	**30**	**130**	**57**	**11**	**Current work**

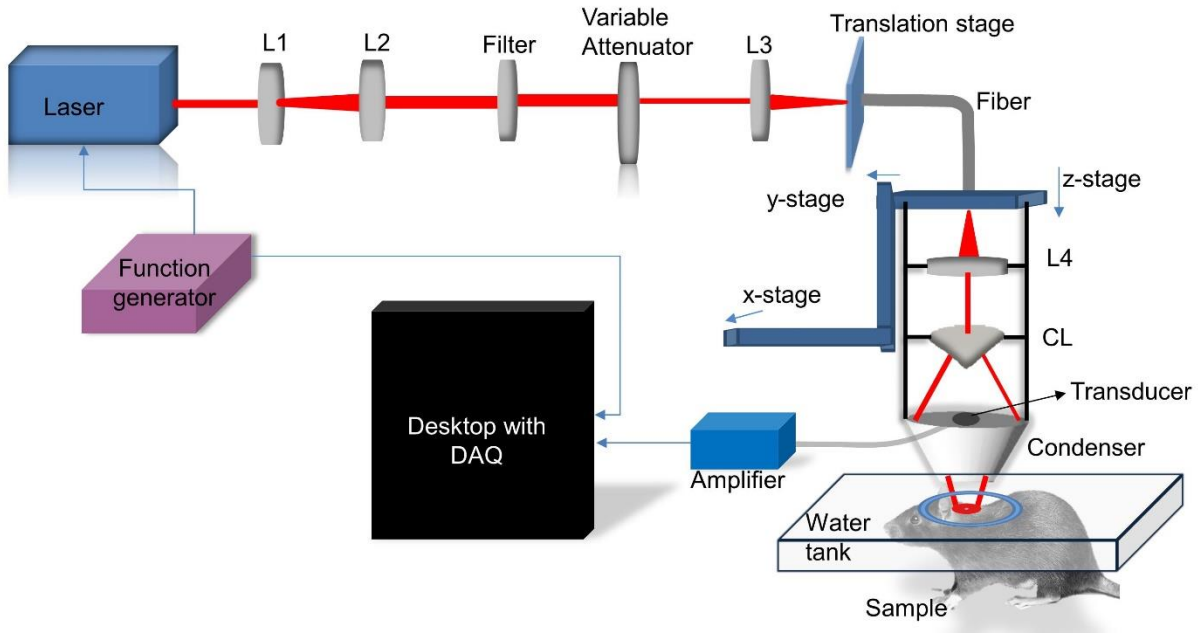

Figure 1. Experimental set-up of the 1064 nm acoustic resolution photoacoustic microscopy. Laser beam from Nd:YAG laser is passed through cylindrical lens (L1), convex lens (L2), harmonic filter to remove 532 nm, variable attenuator, convex lens (L4), conical lens of apex angle 130˚ (CL) and custom made optical condenser. The donut shaped beam illuminates the sample (carbon microsphere, test target, and rat) through the imaging window of the water tank. The ultrasound signals are acquired by the transducer fitted in the condenser and amplified before sending to the computer. The laser excitation and the data acquisition (DAQ) is controlled by the function generator.

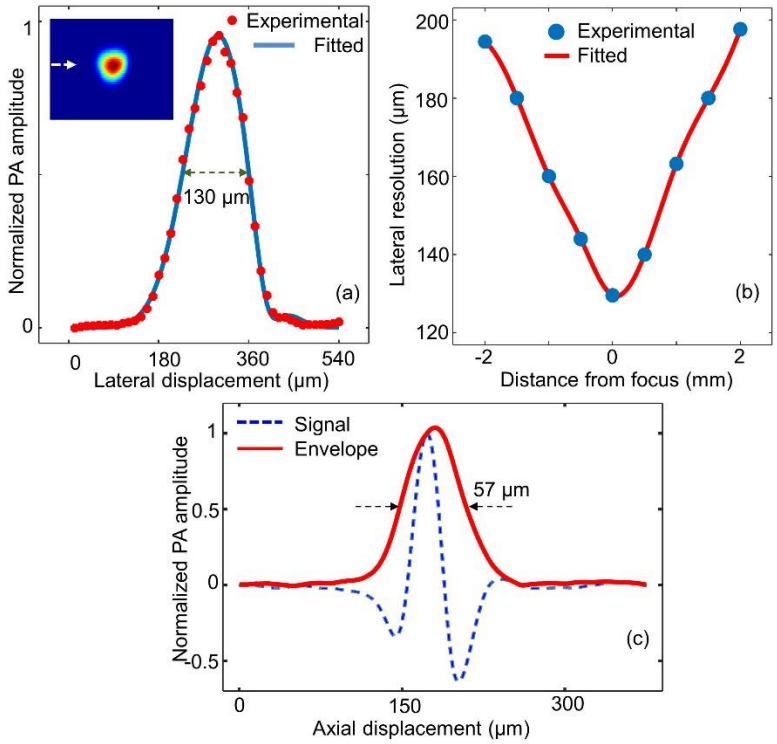

Figure 2. Resolution characterization of 1064-AR-PAM system. (a) Dotted line is the profile at the centre of the microsphere and the solid line is the Gaussian curve fit. Inset is the maximum amplitude projection (MAP) photoacoustic image of the microsphere. The arrow points to the center along which the line profile was taken. (b) The resolution of the microsphere across various depth from the focus. (c) Dashed blue line is the A-line of the photoacoustic signal generated from a carbon microsphere and solid red line is the envelope of the photoacoustic signal.

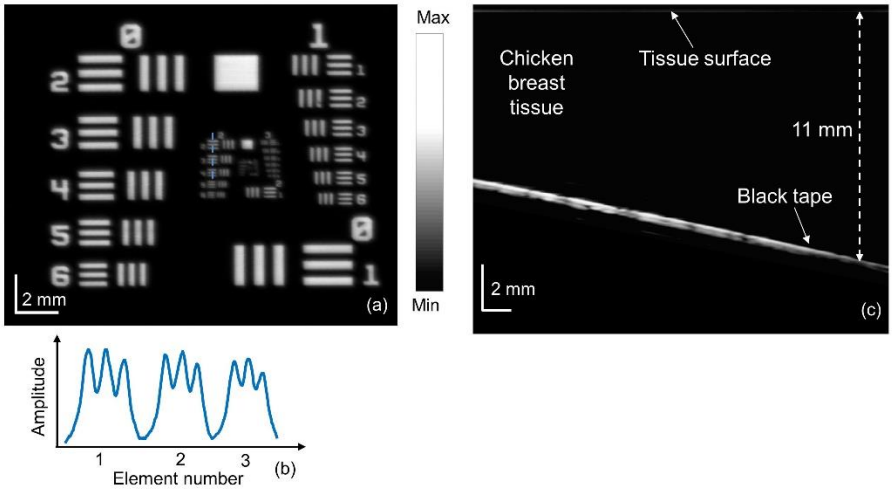

Figure 3. (a) Maximum amplitude projection (MAP) photoacoustic image of USAF (1951) test target over 20 mm ×20 mm area which encloses the groups 0 to 7. (b) Profile of group 2 elements 2-4. (c) Averaged B-scan of the black tape embedded in the chicken breast.

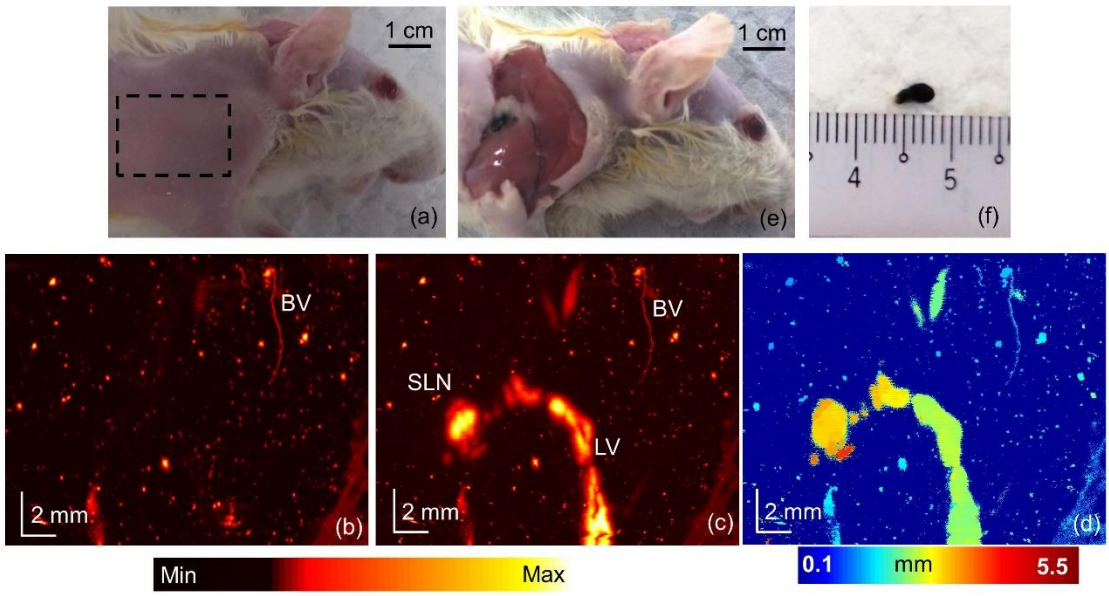

Figure 4. Sentinel lymph node imaging of rat (a) photograph of the animal before injection, the dotted rectangle shows the area of interest, (b) maximum amplitude projection (MAP) photoacoustic image of the pre-injection scan, (c) the sentinel lymph node (SLN), lymph vessel (LV) and blood vessel (BV) are shown in the MAP photoacoustic image after black ink injection. (d) Depth encoded maximum amplitude projection (DE-MAP) image of SLN. (e) Photograph of the animal after the imaging was complete and the animal was euthanized. (f) Dissected SLN for validation with the in vivo image.

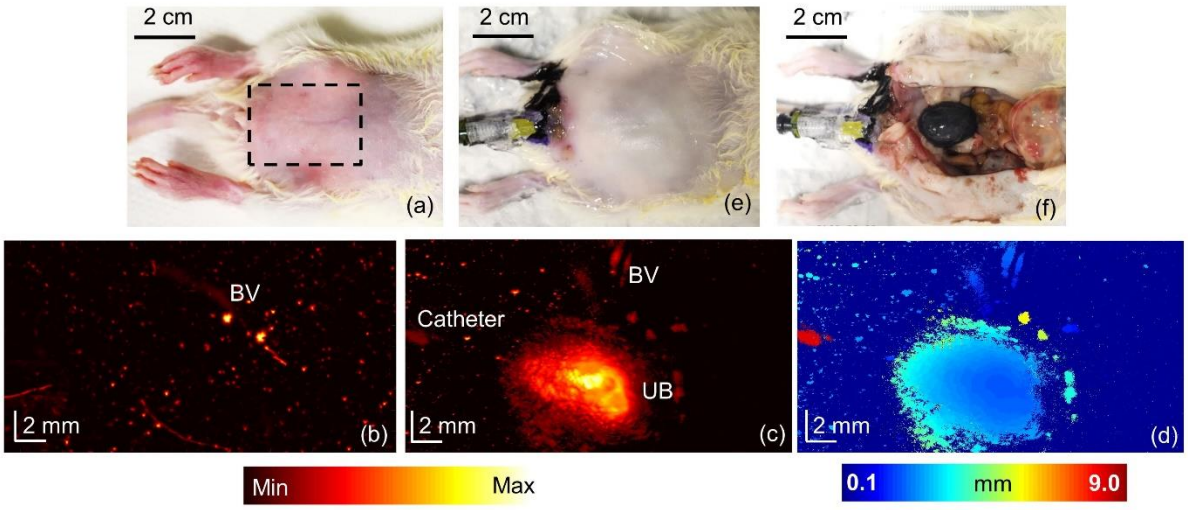

Figure 5. Urinary bladder imaging of rat. (a) Photograph of the animal before injection, the dotted rectangle shows the area of interest, (b) maximum amplitude projection (MAP) photoacoustic image of the pre-injection scan, (c) blood vessel (BV) and urinary bladder are shown in the MAP photoacoustic image after the injection of black ink, (d) depth encoded maximum amplitude projection (DE-MAP) image of urinary bladder, (e) photograph of the animal after the imaging was completed and animal was euthanized, (f) photograph of the dissected urinary bladder.

Graphical abstract:

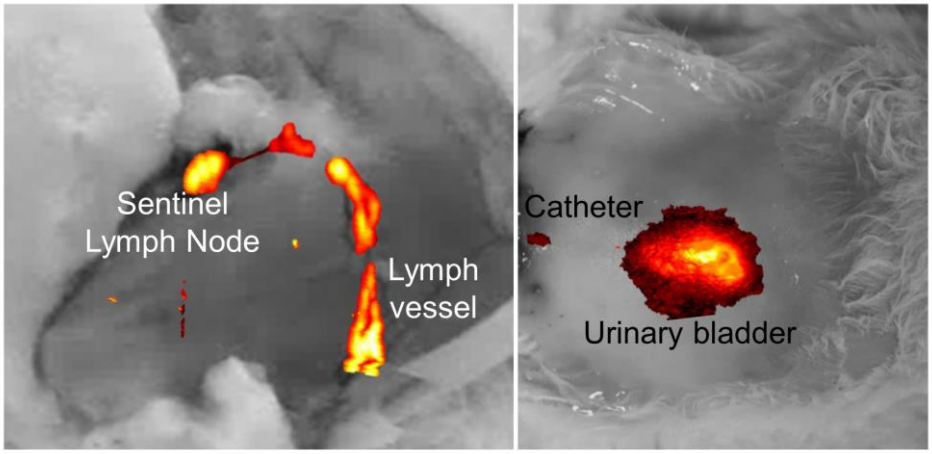

High resolution, high depth acoustic resolution photoacoustic microscopy (1064-AR-PAM) was developed using 1064 nm light excitation. The near infrared - II wavelength enables deeper light penetration. The lateral resolution of the 1064-ARPAM is 130 µm, axial resolution is 57 µm, and this system can image up to 11 mm deep in biological tissues. Sentinel lymph node, lymph vessel, and urinary bladder were imaged in vivo using contrast agent with the developed set-up.